JOURNAL OF SOLID STATE CHEMISTRY **122,** 53–58 (1996)
ARTICLE NO. 0081

Structures in the Oxygen-Deficient Fluorite-Related R_nO_{2n-2} Homologous Series: $Pr_{12}O_{22}$

J. Zhang,* R. B. Von Dreele,† and L. Eyring*

*Department of Chemistry and Biochemistry and the Center for Solid State Science, Arizona State University, Tempe, Arizona 85287-1604; and †Manuel Lujan, Jr. Neutron Scattering Center, LANSCE, MS H805, Los Alamos National Laboratory, Los Alamos, New Mexico 87545

Received January 13, 1995; in revised form November 10, 1995; accepted November 14, 1995

The crystal structure of $Pr_{12}O_{22}$ was determined utilizing Rietveld analysis of powder neutron diffraction data ($P2_1/c$, a = 6.6850(2) Å, b = 11.6004(4) Å, c = 12.8271(4) Å, β = 99.974(1)°, V = 979.67(8) Å^3; total variables 130, R_p = 3.25%, wR_p = 5.02%). This structure is different from the models previously proposed, and the basic structural element is the isolated oxygen vacancy, as observed in another more-oxidized member of the R_nO_{2n-2} series, $Tb_{11}O_{20}$. © 1996 Academic Press, Inc.

INTRODUCTION

In the PrO_x–O_2 system, the β phase with composition Pr_6O_{11} is the most stable intermediate phase at atmospheric oxygen pressure and ordinary temperatures. It can be obtained as a black powder when praseodymium salts are decomposed to the oxide at higher temperatures, then slowly cooled in air (1). Thermodynamic studies established that the β phase has a narrow composition range over a substantial temperature interval. X-ray powder diffraction experiments over its existence region show that it is related to PrO_2 which has the fluorite structure (2–7). As more intermediate phases were discovered, it was also realized that β is the n = 12 member of the Pr_nO_{2n-2} homologous series (4). Critical information was obtained through electron diffraction to establish the unit cell dimensions for β_1 phase (the unit cell content is $Pr_{24}O_{44}$) and its vector relationship with the parent fluorite structure (8). Single crystal X-ray diffraction investigations further determined that the crystal system was monoclinic, and that the space group was $P2_1/n$ for a nonreduced cell (9, 10).

However, further structural studies provided little progress beyond the unit cell level. Attempts at structure determination through conventional single crystal X-ray diffraction were not successful (10) owing to the fact that the specimen might have been twinned and the absorption correction for the X-ray data was crucial and imprecise. As high resolution transmission electron microscopy (HRTEM) became a promising alternative, several efforts were made to derive models for β_1 utilizing image simulation (11–14). Due to technical difficulties, such as beam tilt and dynamic diffraction, the reliability of these models was limited. The low electron scattering cross section for oxygen and the poor stability of the samples in the electron beam also presented serious problems for the HRTEM studies. In addition, the assumption that the oxygen vacancies occurred in pairs in all the intermediate phases confined the search for models to test. Despite the apparent conflict with the symmetry information provided by single crystal X-ray diffraction (9, 10), a $P\bar{1}$ model with vacancy pairs was developed for β_1 based primarily on electron microscopy and image simulation (11–14).

Major progress in structure determination of the rare earth intermediate oxides was made possible due to the improved resolution of neutron powder diffraction at the Los Alamos National Laboratories and the advanced structure refinement package, GSAS (15). Recently, the structures of Pr_9O_{16}, $Pr_{10}O_{18}$, Tb_7O_{12}, and $Tb_{11}O_{20}$ have been determined utilizing Rietveld refinement on the powder neutron diffraction data (16–18). The structure of $Pr_{12}O_{22}$ was also reinvestigated with the neutron powder diffraction data available. This study provides essential information in understanding the defect structure of the rare earth homologous series. Success in solving the baffling structural problem for $Pr_{12}O_{22}$ ($Pr_{24}O_{44}$) once again confirmed the capability of neutron Rietveld refinement in complex structure analyses.

EXPERIMENTAL

Sample preparation. The $Pr_{12}O_{22}$ sample for the powder neutron diffraction study was prepared following procedures previously described (4, 5). The starting material Pr_6O_{11} (Research Chemicals Inc., of 5N purity) was heated to 1000°C for several hours to remove possible contamination from carbonates and hydroxides formed during storage. The product was light green, characteristic of the A-type Pr_2O_3. Based on previous thermodynamic studies, the composition was adjusted by treating the sample under 350 Torr of O_2 at 420°C, and the sample was held under

0022-4596/96 $18.00

TABLE 1
Important Refinement Parameters for β_1 $Pr_{24}O_{44}$

Diffractometer type		NPD
Number data		25976
Minimum d spacing (Å)		0.475 ($2\theta \pm 148°$) 0.480 ($2\theta \pm 90°$)
Model		100% $Pr_{12}O_{22}$
Space group		$P2_1/c$
Lattice constants		
a, b, c (Å)		6.6850(2), 11.6004(4), 12.8271(4)
β (°)		99.974(1)
V (Å^3)		979.69(8)
Z		2
Variables		
Structural	lattice	4
	positional	51
	thermal	2
Other	background	48
	diffractometer	9
	profile (Gaussian)	12
	scale	4
Total		130
wRp %[a]		5.02
Rp %[b]		3.25
χ^2 (reduced)[c]		3.09

[a] $wRp = [w\Sigma(I_O - I_C)^2/\Sigma wI_O^2]^{1/2}$
[b] $Rp = \Sigma|I_O - I_C|/\Sigma I_O$
[c] $\chi_2 = \Sigma w(I_O - I_C)^2/(N_{obs} - N_{cvab})$

these conditions for 10 days to ensure homogeneity and improve crystallinity.

The samples thus prepared were kept in sealed glass tubes until transferred, under an inert atmosphere, into air-tight vanadium cans for neutron diffraction studies.

Neutron diffraction and Rietveld analysis. Time-of-flight (TOF) neutron diffraction data were collected on the high resolution instrument (NPD) and the high intensity (HIPD) instrument at the Manuel Lujan, Jr. Neutron Scattering Center in the Los Alamos National Laboratories.

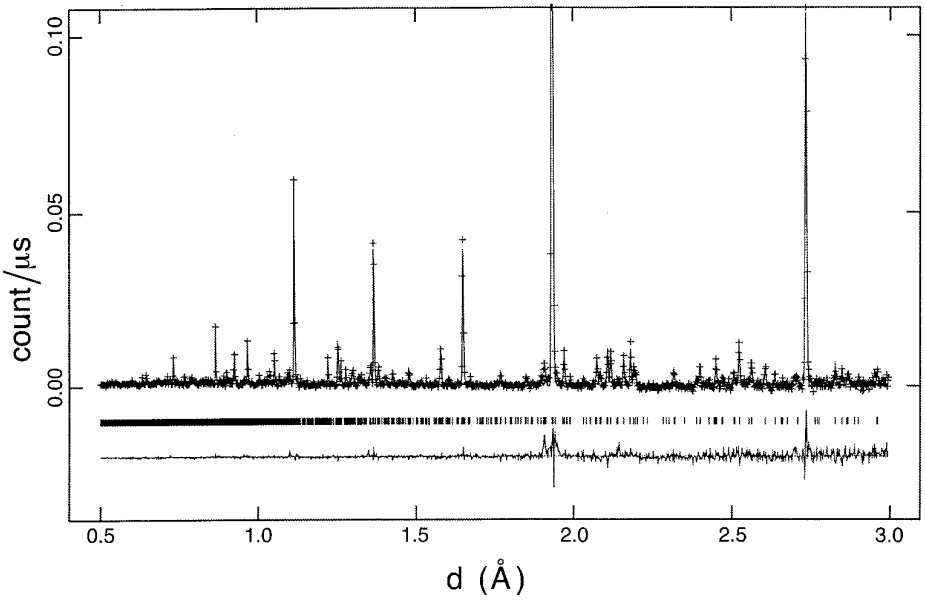

FIG. 1. The observed (crosses) and calculated (solid line) powder neutron diffraction profiles for $Pr_{24}O_{44}$ (β_1). The Bragg positions are marked.

TABLE 2
Positional and Thermal Parameters for β_1 $Pr_{24}O_{44}$

Atom	x	y	z	$U_{iso} \times 100$ (Å^2)[a] (linked)
Pr(1)	0.8607(5)	−0.0136(3)	0.1181(3)	0.63(1)
Pr(2)	0.4095(4)	0.1682(4)	0.1275(2)	0.63(1)
Pr(3)	0.8719(5)	0.3469(3)	0.1235(3)	0.63(1)
Pr(4)	0.8636(5)	0.6670(4)	0.1088(2)	0.63(1)
Pr(5)	0.3736(6)	0.5045(3)	0.1321(3)	0.63(1)
Pr(6)	0.3564(5)	0.8332(4)	0.1275(3)	0.63(1)
O(1)	0.1744(5)	0.0158(3)	0.0762(2)	1.056(9)
O(2)	0.7492(4)	0.1613(3)	0.0775(2)	1.056(9)
O(3)	0.1735(4)	0.3180(3)	0.0876(2)	1.056(9)
O(4)	0.6920(5)	0.5140(2)	0.0540(2)	1.056(9)
O(5)	0.1769(4)	0.6648(3)	0.0579(2)	1.056(9)
O(6)	0.6635(4)	0.8247(3)	0.0473(2)	1.056(9)
O(7)	0.5696(5)	0.0005(2)	0.1762(3)	1.056(9)
O(8)	0.5821(4)	0.3389(3)	0.1814(2)	1.056(9)
O(9)	0.0366(5)	0.5228(3)	0.2059(2)	1.056(9)
O(10)	0.5912(4)	0.6719(3)	0.2040(2)	1.056(9)
O(11)	0.0244(4)	0.8199(3)	0.1925(2)	1.056(9)
$\square_O$	1/16	1/6	3/16	—

[a] The form of the isotropic displacement parameter is $T = \exp[-8\pi^2 U_{iso}\sin^2\theta/\lambda^2]$, where T is the temperature factor.

Using the pulsed neutron source, TOF intensity data were collected at a series of 2θ angles (NPD $\pm 148°$ and $\pm 90°$; HIPD $\pm 153°$, $\pm 90°$, $\pm 39°$, $\pm 14°$, $\pm 5°$, respectively). The subsequent Rietveld refinements were performed utilizing the GSAS structure analysis package (15).

Variables such as background, scale factors, diffractometer constants and profile coefficients were adjusted while using a pseudo fluorite cell as the initial structure model. The cubic symmetry of the fluorite cell was removed, and the lattice constants were refined to fit the strong substructure reflections. Although relatively weak, the superstructure peaks were clearly visible on the difference curve.

Attempts to refine the $P\bar{1}$ model previously proposed (11, 14) was unsuccessful, yielding poor agreement between the observed and the calculated spectra ($wR_p = 7\%$, $\chi^2 = 4.7$) and unreasonably short Pr–O and O–O distances. The refined superstructure lattice parameters showed two angles very close to 90°, strongly suggesting that the crystal system was monoclinic instead of the proposed triclinic.

Efforts were then made to search for better models. Careful examination of a large number of transmission electron diffraction patterns accumulated over the years showed that the reciprocal lattice symmetry corresponded to that of a monoclinic crystal system. Furthermore, many of these patterns shared common systematic weak or absent reflections, which suggested the presence of possible screw axes and/or glide planes. A collection of about a dozen models in a few monoclinic space groups (e.g., $P2_1$, Pc, $P2_1/c$, $P2/c$, $P2_1/m$, etc.) were developed, and an electron diffraction pattern for each of these candidates was calculated, assuming kinematical diffraction conditions. Although many of the calculated patterns resembled the main features of the observed patterns, no completely satisfactory match could be found because the observed patterns were the result of dynamical diffraction and the model input must have been different from the actual structure in certain details.

One of the above models in the space group Pc was

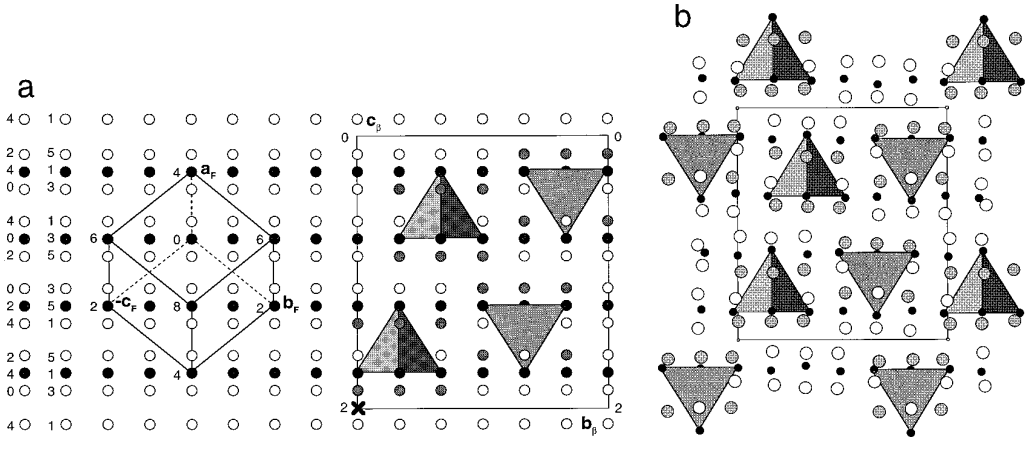

FIG. 2. (a) The vector relationship between β_1 and the parent fluorite structure, and the idealized $\square_O Pr_4O_6$ vacancy clusters viewed along the $[100]_{\beta 1} = 1/2[2\ 1\ \bar{1}]_F$ direction. The integers beside the filled circles representing the metal atoms in the fluorite subcell indicate respectively their heights in 1/6ths of $1/2[2\ 1\ \bar{1}]_F$. The tetrahedral Pr_4 groups around the oxygen vacancies ($\square_O$) are outlined, and the six oxygens involved in each vacancy cluster are shaded. Filled circles, metal atoms; open circles, oxygen atoms. (b) A drawing of the projection of the refined structure of β_1 ($Pr_{24}O_{44}$) along $[100]_{\beta 1} = 1/2[2\ 1\ \bar{1}]_F$. The large circles represent oxygen atoms and the smaller circles praseodymium cations. The tetrahedral Pr_4 groups around the oxygen vacancies ($\square_O$) are outlined, and the six oxygens involved in each vacancy cluster are shaded.

chosen as the starting point for Rietveld analysis. Contrary to the $P\bar{1}$ model, where oxygen vacancies were assumed to occur in pairs, two unique single-oxygen vacancy sites were chosen. A preliminary refinement using one bank of data indicated that the atoms around one of the oxygen vacancies behaved normally, yet those around the other had experienced large shifts. Examination of the distances suggested that the second vacancy had been misplaced. The correct solution should be a model with $P2_1/c$ symmetry, and the four single oxygen vacancies in each unit cell should be related by symmetry.

Further refinement of this modified model with one bank of the NPD data went smoothly. The model was also tested with the HIPD data, yielding essentially the same results. Since the NPD data were sufficient for the full refinement, the HIPD data were not included in further trials. In the final stage of the refinement all four banks of data collected on NPD were included to improve the quality of the solution. This led to satisfactory refinement parameters (Table 1) and a significant decrease in the standard deviations and the magnitudes of the thermal parameters (Table 2). The calculated spectra are in good agreement with those observed (see Fig. 1). The important distances reported in Table 3 are reasonable with the shortest O–O and Pr–O distances being 2.656(4) Å and 2.153(5) Å, respectively. These values are comparable to the values observed in the other intermediate praseodymium oxides, which ensures the reliability of the structure model.

RESULTS AND DISCUSSION

The present neutron powder diffraction study confirmed the relationship of β_1, $Pr_{24}O_{44}$, to the parent fluorite to be

$$a_{\beta 1} = 1/2\,(2a_F + b_F - c_F)$$
$$b_{\beta 1} = 3/2\,(\quad + b_F + c_F)$$
$$c_{\beta 1} = 1/2\,(2a_F - 3b_F + 3c_F),$$

and the corresponding space group to be $P2_1/c$. This vector relationship is represented graphically in Fig. 2a. Taking

$$c_{\beta 1'} = -a_{\beta 1} + c_{\beta 1} = -2b_F + 2c_F,$$

this cell can be translated to the Kunzmann cell established through electron diffraction (8). This operation also transforms the symmetry into the nonstandard setting, $P2_1/n$, which was previously reported for β_1 based on single crystal X-ray diffraction (9, 10). Furthermore, the refined lattice constants are in good agreement with those obtained from powder X-ray diffraction data.

The present study also succeeded in determining the structure of β_1 with accuracy at the atomic level. Figure 2a shows the relationship between the fluorite subcell and the ideal supercell. Figure 2b is a drawing of the projection of the refined structure of $Pr_{24}O_{44}$ along $[100]_{\beta 1}$. The most significant difference between this structure and the previ-

TABLE 3
Important Interatomic Distances in β_1 $Pr_{24}O_{44}$

Atom 1	Atom 2	Distance (Å)	Atom 1	Atom 2	Distance (Å)
		Pr coordination environment			
Pr(1)	O(1)	2.462(5)	Pr(2)	O(1)	2.381(5)
CN7[a]	O(1)	2.279(5)	CN7	O(2)	2.466(4)
[+4][b]	O(2)	2.193(5)	[+4][b]	O(3)	2.343(5)
	O(6)	2.380(5)		O(6)	2.211(4)
	O(7)	2.208(6)		O(7)	2.256(6)
	O(9)	2.283(5)		O(8)	2.335(5)
	O(11)	2.340(5)		O(10)	2.162(4)
	Ave.	2.306(5)		Ave.	2.308(5)
Pr(3)	O(2)	2.344(5)	Pr(4)	O(3)	2.495(4)
CN7	O(3)	2.170(5)	CN7	O(4)	2.153(5)
[+4][b]	O(4)	2.372(4)	[+4][b]	O(5)	2.300(4)
	O(5)	2.297(5)		O(6)	2.323(6)
	O(8)	2.194(5)		O(9)	2.277(5)
	O(9)	2.467(5)		O(10)	2.362(4)
	O(11)	2.363(4)		O(11)	2.249(5)
	Ave.	2.315(5)		Ave.	2.310(5)
Pr(5)	O(3)	2.555(5)	Pr(6)	O(1)	2.475(5)
CN8	O(4)	2.361(5)	CN8	O(2)	2.602(4)
[+3][b]	O(4)	2.508(6)	[+3][b]	O(5)	2.383(6)
	O(5)	2.379(6)		O(6)	2.453(5)
	O(7)	2.422(5)		O(7)	2.424(5)
	O(8)	2.393(6)		O(8)	2.415(5)
	O(9)	2.599(6)		O(10)	2.529(5)
	O(10)	2.505(5)		O(11)	2.507(5)
	Ave.	2.465(6)		Ave.	2.474(5)
		$\square_O Pr_4O_6$ vacancy cluster			
$\square_O$	Pr(1)	2.563(4)	Pr(1)	Pr(2)	4.215(5)
	Pr(2)	2.568(3)		Pr(3)	4.184(3)
	Pr(3)	2.511(3)		Pr(5)	4.221(4)
	Pr(4)	2.573(3)	Pr(2)	Pr(3)	4.141(4)
	Ave.[c]	2.554(3)		Pr(5)	4.112(4)
			Pr(3)	Pr(5)	4.144(4)
	O(1)	2.456(3)	Ave.[c]		4.170(4)
	O(2)	2.315(3)			
	O(3)	2.367(3)			
	O(9)	2.326(3)			
	O(10)	2.486(3)			
	O(11)	2.485(3)			
	Ave.	2.406(3)			

Summation of crystal radii (Å)[d]

Pr^{m+}	CN = 7	CN = 8
$m = 3$	2.44	2.506
$m = 4$	2.29	2.34

[a] CN is the coordination number.
[b] The charges are assigned by comparing the average distances with the corresponding summation of crystal radii (21).
[c] The value is the average within the $\square_O Pr_4O_6$ cluster.
[d] Values are from reference (20).

ous models is the absence of the oxygen vacancy pairs, such as those observed in Pr_7O_{12}, Pr_9O_{16}, and $Pr_{10}O_{18}$. Instead, single oxygen vacancies are observed and they are distributed in the lattice in a uniform pattern.

It has been shown that the various structures of intermediate rare earth oxides may be built with a simple basic defect cluster, $\square_0R_4O_6$, introduced first by Martin (16, 19). This defect cluster is created when an oxygen atom is extracted from the parent fluorite structure RO_2, and it involves the vacant R_4 tetrahedron and its six edge-bridging oxygen atoms (Fig. 2a). The validity of this concept was confirmed by the structure of β_1. In β_1, due to the positive local charge introduced by the creation of a vacant oxygen site, the six surrounding oxygens are drawn toward the center of the defect by 0.3 Å while the four neighboring cations are shifted away by about 0.2 Å. Since these shifts represent the most significant distortions from the ideal fluorite structure, the atoms involved are considered as a group, namely as a defect cluster or a coordination defect.

Consistent with the known structures of other intermediate phases, the structural features of β_1 indicate that the dominant chemical force in the rare-earth oxides is ionic in nature. The electrostatic repulsion between the defect clusters tends to separate them. Oxidation in these systems results in a systematic increase in the spatial separation of the vacancies. The apparent structural differences between intermediate phases with various oxidation states may be rationalized on this basis. For the more reduced intermediate phases in the R_nO_{2n-2} homologous series (n = 7, 9, 10), the defect clusters occur in pairs by sharing a common metal atom, i.e., $(\square_0R_{3+1/2}O_6)_2$ (16, 17, 20), and the distance between he two vacancies within a pair is $1/2\langle 111\rangle_F$. The vacancy pairs are preserved in oxidation of Pr_7O_{12} to Pr_9O_{16} or $Pr_{10}O_{18}$ although the distances between them are necessarily increased. Breaking up these pairs would lead to less favorable arrangements (16). As the concentration of the vacant oxygen sites is further decreased in the higher oxides, such as in $Pr_{24}O_{44}$ and $Tb_{11}O_{20}$, it becomes possible and even favorable to eliminate all the short vacancy–vacancy distances including the $1/2\langle 111\rangle_F$ connections within a vacancy pair. Structures with isolated vacant oxygen sites are thus formed. The shortest vacancy–vacancy distances in β_1 as well as in $Tb_{11}O_{20}$ are $1/2\langle 210\rangle_F$.

Beyond the rule of "maximum separation of defect clusters," the relaxation of the intercluster cation sublattice is also of importance. With the distances between the vacancies fixed, two possible models of the single cluster structure may be derived when the cation lattice is taken into consideration. As shown in Fig. 3, these two models are different from each other in the relative positions of the Pr sublattice with respect to the vacancies. The fact that β_1 adopts model 3a rather than 3b implies that the former

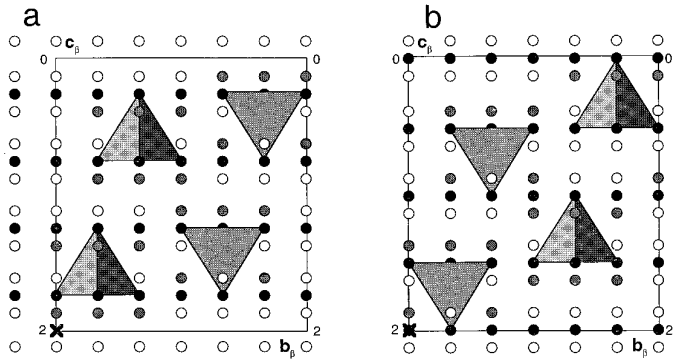

FIG. 3. Comparison of two models for β_1 with different matrices viewed along $[100]_{\beta 1}$ direction. The atom positions are idealized (see text). The origins of the unit cells are marked as crosses.

is relatively more stable. This difference in stability may be rationalized when the cations in β_1 are divided into two groups. The first group of Pr cations are those participating in the $\square_0Pr_4O_6$ vacancy cluster (Pr(1) to Pr(4), CN = 7). An average Pr–O distance of 2.31 Å (Table 3) requires the formal charge on these Pr ions to be +4. The second type of Pr cations are those without an oxygen vacancy in their first coordination sphere and the average Pr–O distances suggest a formal charge of +3 on the Pr ion. The result of the cation lattice relaxation is that the intracluster Pr–Pr distances have an average of 4.1 Å, while the intercluster Pr–Pr distances are about 0.4 Å shorter. In other words, the Pr^{3+} ions are crowded into the region between the defect clusters. With a composition of $Pr^{3+}O_2^{2-}$, this second type of Pr cation and its oxygen neighbors form a negatively charged zone, serving as a buffer separating the positively charged defect clusters. The more uniform distribution of the second type of Pr cations in model 3a is apparently more effective in shielding the vacancy clusters and reducing lattice tension.

As demonstrated for $Pr_{10}O_{18}$ (17), the structure of β_1 may also be viewed as a stacking of $(0\ 2\ \bar{2})_F$ planes along the b_β axis. Within the β_1 cells, there are four $(0\ 2\ \bar{2})_F$ planes with composition $Pr_4O_7\square_O$ (plane A) and two with composition Pr_4O_8 (plane B). The refined structure of β_1 possesses a stacking sequence of ($AABAAB$) or (110110) where the integers denote the number of vacancies on each plane. Compared to the $P\bar{1}$ model, previously proposed (11, 14), which has the stacking sequence of ($AAAABB$) or (111100), the β_1 structure refined here represents a more uniform distribution of the $(0\ 2\ \bar{2})_F$ planes along the b_β direction. The established structures of β_1 and the other intermediate rare earth oxides suggest that a uniform distribution of different structural elements is a general rule for systems with strong ionic character. These observations may serve as general guidelines in evaluating structural models for similar systems.

CONCLUSIONS

The structure of β_1, $Pr_{24}O_{44}$ has been determined through powder neutron, TOF, diffraction, and Rietveld analysis. The unit cell for β_1 is monoclinic with $P2_1/c$ symmetry. The basic structural element is the single $\square_O Pr_4O_6$ vacancy cluster similar to those found in $Tb_{11}O_{20}$ where the shortest vacancy separation is also $1/2\langle 210\rangle_F$. The lattice distortion with respect to the fluorite structure suggests that the defect clusters are positively charged, and are distributed in a uniform pattern, following the common rules observed in the other members of the R_nO_{2n-2} homologous series of rare earth oxides.

ACKNOWLEDGMENT

It is a pleasure to acknowledge the patient tutorial help of D. J. M. Bevan in understanding the intricacies of these complex fluorite-related structures. Helpful discussions with E. Schweda are gratefully acknowledged. We thank the National Science Foundation for financial support through Research Grant DMR-9114799 and the Office of Basic Energy Sciences Division of Materials Sciences of the U.S. Department of Energy (Contract W-7405-ENG-36).

REFERENCES

1. L. Eyring, *in* "Handbook on the Physics and Chemistry of Rare Earths" (K. A. Gschneidner, Jr. and L. Eyring, Eds.), Vol. 3, p. 337. North-Holland, Amsterdam, 1979; and R. G. Haire and L. Eyring, "Handbook on the Physics and Chemistry of Rare Earths" (K. A. Gschneidner, Jr. and L. Eyring, Eds.), Vol. 18, p. 413. North-Holland, Amsterdam, 1994.
2. R. E. Ferguson, E. D. Guth, and L. Eyring, *J. Am. Chem. Soc.* **76,** 3890 (1954).
3. B. G. Hyde, D. J. M. Bevan, and L. Eyring, *in* "Rare Earth Research II" (K. S. Vorres, Ed.), p. 277–296. Gordon and Breach, New York, 1964.
4. J. M. Honig, A. F. Clifford, and P. A. Faeth, *Inorg. Chem.* **2,** 791 (1963).
5. B. G. Hyde, D. J. M. Bevan, and L. Eyring, *Phil. Trans. R. Soc. London, Series A* **259,** 583 (1966).
6. J. O. Sawyer, B. G. Hyde, and L. Eyring, *Bull. Soc. Chim. France* **149,** 152 (1965).
7. D. A. Burnham and L. Eyring, *J. Phys. Chem.* **72,** 4415 (1968).
8. P. Kunzmann and L. Eyring, *J. Solid State Chem.* **14,** 229 (1975).
9. M. Z. Lowenstein, L. Kihlborg, K. H. Lau, J. M. Haschke, and L. Eyring, *NBS Spec. Pub.* **364,** 344 (1972).
10. R. T. Tuenge, R. B. Von Dreele, and L. Eyring, "Proceedings of the 12th Rare Earth Research Conference, Vail, Colorado, July 18–20, 1976." p. 594. 1976.
11. E. Summerville, R. T. Tuenge, and L. Eyring, *J. Solid State Chem.* **24,** 21 (1978).
12. E. Schweda and L. Eyring, *Ultramicroscopy* **23,** 443 (1987).
13. E. Schweda and L. Eyring, *J. Solid State Chem.* **78,** 1 (1989).
14. E. Schweda, D. J. M. Bevan, and L. Eyring, *J. Solid State Chem.* **90,** 109 (1991).
15. A. C. Larson and R. B. Von Dreele, "GSAS-General Structure Analysis System." Los Alamos National Laboratory Report LA-UR 86-748 (1990).
16. J. Zhang, R. B. Von Dreele, and L. Eyring, *J. Solid State Chem.* **118,** 133 (1995).
17. J. Zhang, R. B. Von Dreele, and L. Eyring, *J. Solid State Chem.* **118,** 141 (1995).
18. J. Zhang, R. B. Von Dreele, and L. Eyring, *J. Solid State Chem.* **104,** 21 (1993).
19. R. L. Martin, *J. Chem. Soc. Dalton* 1335 (1974).
20. R. B. Von Dreele, L. Eyring, A. L. Bowman, and J. L. Yarnell, *Acta Crystallogr. Sect. B* **31,** 971 (1975).
21. R. D. Shannon, *Acta Crystallogr. Sect. A* **32,** 751 (1976).